

# Data-Driven Lifetime Risk Assessment and Mitigation Planning for Large-Scale Satellite Constellations

**Paul Diaz, Pol Mesalles Ripoll, Matthew Duncan**

*SpaceNav*

**Mike Lindsay, Toby Harris**

*Astroscale*

**Hugh G. Lewis**

*University of Southampton*

## ABSTRACT

We introduce a methodology for estimating the risk posed to the space environment by a spacecraft over an arbitrary period of time following a risk mitigation strategy, in terms of aggregate collision probability. Our methodology enables estimation of residual risk and maneuver frequency, where residual risk is defined conceptually as the risk to a spacecraft which remains even after adherence to a risk mitigation strategy. The key parameters considered which affect residual risk for a general risk mitigation strategy are the risk mitigation maneuver (RMM) threshold, the risk reduction factor, and the maneuver execution time. We present an analytic result regarding the necessary residual risk (per-satellite) to ensure the total aggregate collision probability of a satellite constellation of arbitrary size be below a target value. This approach offers a more complete model of spacecraft safety and potential risk to the space environment by studying more than just the RMM threshold, which has historically been used as a common benchmark in space situational awareness and regulatory compliance literature. Our analysis shows that the RMM threshold is but one of a few factors which have significant effects on residual risk. We provide evidence that the RMM threshold alone is an incomplete indicator of the actual risk posed to the space environment by an operational spacecraft. We demonstrate the effectiveness of this methodology by presenting numerical results which model realistic satellites and satellite constellations and draw key insights from this analysis which will aid in managing the safety and sustainability of the space environment and inform risk mitigation strategies for large satellite constellations.

## 1. INTRODUCTION

In an era dominated by commercial aerospace, the number of proposed and deployed satellite constellations in Low Earth Orbit (LEO) is likely to increase in the near-future [17]. Companies such as SpaceX, OneWeb, Amazon (Kuiper), Telesat, Astra Space, Boeing, Hughes Network Systems, SpinLaunch/SN Space Systems, Inmarsat, Intelsat, the Chinese state-owned company Guangwang, and the Rwandan Government (Cinnamon-937), all either have existing large-scale satellite constellations deployed, have plans to deploy large satellite constellations, or have plans to expand their existing satellite constellations [19, 28, 5, 9, 26]. In the two years prior to 2021-03-30, the number of active and inoperative satellites in LEO increased by more than 50 % to approximately 5000 [4]. Among the most ambitious proposals are SpaceX's with aims to launch 34 408 satellites, and the government of Rwanda proposing to launch 327 320 satellites.

Given the ongoing growth of the orbital debris population and the unprecedented growth in the number of large satellite constellations or so-called "mega-constellations", there is a great need to understand and quantify the potential risk posed to the space environment for all operational satellites, but particularly for member satellites of mega-constellations. This need is acutely relevant due to the ongoing evolution of different regulatory requirements, or in some cases recommended guidelines, being imposed by different governing bodies or regulatory agencies across multiple countries such as the United States Federal Communications Commission (FCC), the International Telecommunications Union (ITU), or the Inter-Agency Space Debris Coordination Committee (IADC) [21].

The Outer Space Treaty (OST), ratified by the United Nations Committee for the Peaceful Uses of Outer Space (COP-UOS) in 1967, offers little to no international legislation for commercial access to space, as it was more concerned

with international security at the height of the Cold War, and originally suggested that commercial activity in outer space was unlikely [3]. As a result, the OST calls for state-lead “authorization and continuous supervision” of all national space activities regardless of those activities being in the public or private interest [24]. It follows that the current state of affairs comprises of a patchwork of governing or regulatory bodies with varying requirements and processes for authorization or continuous supervisions. The major topic discussed in this paper addresses quantities which have been historically used by regulatory agencies like the FCC either as an indicator of regulatory compliance or benchmark of risk posed to the space environment [21].

Perhaps the single most referenced quantity of interest from a regulatory, operations, and safety context is often referred to as the *risk mitigation maneuver (RMM)* threshold,  $P_m$ . The RMM threshold is used operationally to decide whether an RMM is executed by the satellite to avoid a potential collision whenever the collision probability  $P_c > P_m$ . It follows that adopting a more aggressive risk posture by choosing a smaller value of  $P_m$  poses less overall risk to the spacecraft and space environment by opting to perform more RMMs, compared to a larger value of  $P_m$ . It is from this perspective that the RMM threshold  $P_m$  is used as a proxy for measuring potential risk to the space environment.

In this work, we present a methodology for estimation of residual risk and maneuver frequency, where residual risk is defined conceptually as the risk to a spacecraft which remains even after adherence to a risk mitigation strategy. The key parameters considered which affect residual risk for a general risk mitigation strategy are the RMM threshold,  $P_m$ , the risk reduction factor,  $\rho$ , which determines how much collision probability is reduced due to an RMM, and the maneuver execution time,  $\Delta t_{TCA}$  which is the minimum amount of time from a conjunction event for which an RMM decision must be made. We present analysis regarding the necessary residual risk (per-satellite) to ensure the total aggregate collision probability of a satellite constellation of arbitrary size be below a target value. This methodology offers a more complete model of spacecraft safety and potential risk to the space environment by studying more than just the RMM threshold, which has historically been used as a common benchmark in space situational awareness and regulatory compliance literature. Our analysis shows that  $P_m$  is but one of a few factors which have significant effects on residual risk. As such, we demonstrate that the RMM threshold alone is an incomplete indicator of the actual risk posed to the space environment by an operational spacecraft. We demonstrate the effectiveness of this methodology by presenting numerical results which model realistic satellites and satellite constellations, and draw key insights from this analysis which will aid in managing the safety and sustainability of the space environment and inform risk mitigation strategies for large satellite constellations.

Our analysis considers hypothetical satellite constellations modeled on the AQUA and ICESat-2 satellites. The AQUA and ICESat-2 satellites are quite different in terms of mean orbital altitude and serve as low-drag and high-drag LEO scenarios, respectively. The main constellation parameters assumed in our analysis are presented in Table 1.

Table 1: Orbital parameters of analyzed missions.

<b>Mission</b>	<b>Apoapsis [km]</b>	<b>Periapsis [km]</b>	<b>Inclination [°]</b>	<b># of Planes</b>	<b># of Satellites per Plane</b>
AQUA	702.8	701.2	98.2°	50	50
ICESat-2	482.0	479.8	92.0°	50	50

The analysis we present focuses on the on-orbit duration phase of a satellite’s operational lifetime. We focus on the on-orbit duration phase as opposed to the orbit raising/launch or the post-mission disposal (PMD) phases, because satellites spend the overwhelming majority of their operational lifetime (typically years) in this phase and accumulate the majority of their risk to space environment during this time. That is not to say that the launch and PMD phases should be ignored in terms of their risk posed to the space environment by any means, in fact there are a number of studies on these phases specifically [2, 31, 8, 6, 35, 29, 30], but they are considered outside the scope of this analysis.

## 2. A DESCRIPTION OF THE COMPUTATIONAL MODEL

The computational model featured in this document is part of SpaceNav’s Close Approach Service (CAS). This service is designed to model interactions between arbitrary constellations of primary and secondary satellites. In this analysis, collision probabilities and maneuver frequency estimates are created by pairing simulated conjunction events with real covariance data obtained from Conjunction Data Messages (CDMs). A brief description of the main steps of this

process which simulates conjunction events is provided in this section.

## 2.1 Primary Constellations

We consider two primary constellations based on the AQUA and ICESat-2 satellites. Fifty orbital planes are defined equally spaced in right ascension of ascending node (RAAN) values. For each orbital plane, fifty satellites per plane are defined equally spaced in true anomaly. Values of altitude, eccentricity, and inclination are data-driven and obtained from Space-Track.org. Both primary constellations assume  $B^*$  (BSTAR) equals 0 to mimic the effects of station keeping. The result of this construction are primary constellations which consist of a large number of individual satellites. If  $N_p$  is the number of orbital planes and  $N_{spp}$  is the number of satellites per plane, then the total number of satellites in each primary constellations is  $N_p \times N_{spp} = 2500$ . The constellation planes are spaced in RAAN according to  $\delta\Omega = \frac{360^\circ}{N_p+1}$  where the first plane has a RAAN equal to  $0^\circ$ . The true anomaly for the  $j^{\text{th}}$  satellite in the  $i^{\text{th}}$  plane is

$$v_{i,j} = (i-1)v^* + (j-1)\delta v, \quad \text{where} \quad \delta v = \frac{360^\circ}{N_{spp}}, \quad \text{and} \quad v^* = \frac{360^\circ}{N_{spp} \cdot N_p} \quad \text{is the true anomaly offset.} \quad (1)$$

## 2.2 Secondary Constellation

The secondary constellation comprises of the catalog of all tracked real objects larger than 10 cm, for a specified date. For this analysis, historic generalized perturbation (GP) element data was retrieved from Space-Track.org and pre-processed to select unique objects which make up the secondary constellation used in the simulation. Specifically, GP element data with creation dates between 2022-04-23 to 2022-05-04 was obtained from Space-Track.org and pre-processed to select each unique object present in the catalog over the queried data.

## 2.3 Propagation

Using the orbital information in the form of two-line elements (TLEs), defined by the primary and secondary constellations, ephemerides are created via the simplified general perturbation model 4 (SGP4) propagator [20, 34].

## 2.4 Close Approach Prediction

Following propagation, each primary ephemeris was screened against all of the secondary ephemerides to compute conjunction events. The screening compares the ephemerides in vector form, approximates the time of closest approach (TCA) via Lagrange interpolation, and computes the relative miss and velocity geometries for each event. Only events with miss distances in a  $[\pm 2000, \pm 25000, \pm 25000]$  m radial, in-track, cross-track (RIC) volume were considered. This is the standard screening volume for external ephemerides used by the 18<sup>th</sup> Space Defense Squadron (SDS) [1]. For each close approach event the following information is recorded: TCA, primary object name and NORAD CAT ID (if available), secondary object name, NORAD CAT ID, object type, and radar cross section (RCS) size, primary-centered relative miss vector geometry, primary-centered relative velocity vector geometry, and primary and secondary GP element data.

The goal of the process described above is two-fold. First, the process provides a means for estimating the conjunction event frequency of the primary satellites. And second, the process provides relative RIC miss and velocity distributions. Specifically, the distribution of relative position and velocities at the TCA, expressed in the radial, in-track, and cross-track frame, centered at the primary. The simulated distribution of miss geometries enables the computation of a larger set of close approach events for probabilistic risk assessment without the need for additional simulation of close approach events. This larger set of simulated events allows for a better estimation of the frequency of high collision probability events, which is tied directly to the maneuver frequency and residual risk of the mission.

One key assumption for this type of analysis is the concept of sufficient exposure time. There are generally two approaches to achieve sufficient exposure time: (1) simulate a single primary over a large time interval, or (2) simulate a constellation of primaries over a relatively small time interval. This analysis adopts the methodology of (2). It must be determined that the exposure time (defined as the number of primaries  $\times$  propagation time of the CAS simulation) is sufficient to obtain accurate estimates of the event frequency and RIC miss geometry distributions. The numerical simulations presented in this work have been validated to achieve sufficient exposure time by measuring Monte Carlo convergence of event frequency and the differences in the RIC miss distributions with respect to propagation time by using the Jensen–Shannon (JS) divergence [25, 10], the Kruskal–Wallis (KW) test [11], and the two-sample Kolmogorov–Smirnov (KS) test [7]. However, the validation of sufficient exposure time on the CAS simulation is not to main scope of this analysis and for brevity these results are not discussed in great detail in this work.

## 2.5 Covariance Generation

Covariance data is necessary for computation of collision probabilities that enable maneuver frequency and residual risk estimation. SpaceNav maintains a database of historical events for customers with satellites in multiple orbital regimes. In our analysis, we consider the historical CDM data for the AQUA and ICESat-2 satellites. These historical events contain covariance data based off of precision orbits from the 18<sup>th</sup> SDS and therefore form distributions of realistic covariances for the primaries and secondaries, as seen by these satellites in an operational environment.

## 2.6 Post-Processing, Collision Probability, and Maneuver Statistics Computation

SpaceNav performs risk assessment through collision probability ( $P_c$ ) estimates using the results of the CAS simulation. This process is done through Foster's method [14]. Collision probability computations rely on the RIC relative miss geometry distribution, specifically the position and velocity vectors for the primaries and secondaries, and the event frequency distribution. The position vectors, velocity vectors, and event frequency distribution are obtained by post-processing the simulated conjunction events. The event frequency distribution is formed by calculating the number of conjunction events per day per primary satellite, and during  $P_c$  computations the number of events per day per satellite is sampled directly from the empirical event frequency distribution computed during post-processing.

In order to calculate maneuver frequency statistics, a sequence of  $P_c$  values must first be computed. To create this sequence, the primary and secondary position and velocity vectors for each of the simulated conjunction events are paired with historical primary and secondary uncertainty data. We define *propagation time*  $\Delta t_{TCA}$  as the TCA minus the last observation time of the object. The uncertainty data is randomly sampled from the appropriate uncertainty distribution based on propagation time  $\Delta t_{TCA}$ , secondary object RCS size, and secondary object type. Primary uncertainty data is sampled from the primary distribution according to  $\Delta t_{TCA}$  only. Different propagation time bins mimic the effects of different maneuver execution times, e.g., 0–4 hours, 4–8 hours, 8–12 hours, etc., and allow for quantifying the effects of  $\Delta t_{TCA}$  on the maneuver frequency. Upon pairing each conjunction event's primary and secondary position and velocity state vectors with sampled covariance data, collision probability for each simulated conjunction event is calculated. These values of  $P_c$  form the sequences of collision probabilities used in a Monte Carlo method to estimate maneuver frequency and residual risk statistics.

Maneuver frequency is estimated via a Monte Carlo method. The main parameters of these Monte Carlo estimates are: (1) a time interval defined by a number of days, and (2) a number of samples. Maneuver frequency statistics are computed with respect to the time interval and each Monte Carlo sample represents one estimate of the time interval, i.e., the maneuver frequency rate is defined as the number of maneuvers per time interval (e.g., one year). For each Monte Carlo sample, values are drawn from the event frequency distribution to determine the number of events over the time interval, then a sequence of  $P_c$  values is computed by drawing a corresponding number of conjunction events from the simulated set of conjunction events and pairing those events with data-driven covariance values. For any event, if the value of  $P_c$  exceeds the defined risk mitigation maneuver threshold, a given event is considered to have triggered an avoidance maneuver. The main steps of the Monte Carlo estimation method are outlined below for clarity:

1. Let  $n_j$  be the number of events on day  $j = 1, \dots, N_{\text{days}}$ . For each day in the time interval up to  $N_{\text{days}}$ ,  $n_j$  is randomly sampled from the simulated event frequency distribution to generate a sequence of values  $\{n_j\}_{j=1}^{N_{\text{days}}}$ .
2. For the  $j^{\text{th}}$  simulated day,  $n_j$  conjunction events are randomly sampled from the set of simulated conjunction events, which provides the relative geometries, secondary object types, and secondary RCS sizes.
3. Pair each of the sampled conjunction events with covariance data and compute  $P_c$  values. The covariance data is randomly sampled from a set of historical data based on the maneuver execution time(s) ( $\Delta t_{TCA}$ ) of interest, secondary object RCS size, and secondary object type.
4. Compute an estimate for the simulated time interval (Monte Carlo sample), e.g., count the number of events where  $P_c > P_m$  and divide the total by  $N_{\text{days}}$  to estimate maneuver frequency.

For each Monte Carlo sample, counting the number of  $P_c$  values exceeding the risk mitigation maneuver threshold and dividing by the number of days in the time interval  $N_{\text{days}}$  provides a single estimate for maneuver frequency over the specified time interval. Using a large number of Monte Carlo samples, maneuver frequency statistics, such as average unremediated risk, maneuver rate, and residual risk may be computed. In this analysis, the number of days in the time interval was defined as 365 days, and the number of Monte Carlo samples used was 2400, i.e., the maneuver

frequency statistics result from 2400 independently simulated years. For each Monte Carlo sample, we also considered computing yearly aggregate collision probability and residual risk which is described in §2.7.

## 2.7 Residual Risk Estimation

We follow the concepts and notation presented in [18]. Let

$$\mathcal{P} = \{P_{c,i}\}, \quad i = 1, \dots, N \quad (2)$$

be a sequence of simulated collision probabilities, for  $N$  samples, spanning a time period  $T$ . The survival probability for the  $i^{\text{th}}$  event is

$$S_{c,i} = 1 - P_{c,i}, \quad (3)$$

and the total aggregate (or cumulative) survival probability is

$$S_{agg}^{total} = S_{agg}(\mathcal{P}) = \prod_{i=1}^N [S_{c,i}] = \prod_{i=1}^N [1 - P_{c,i}]. \quad (4)$$

Similarly, the *total aggregate (or cumulative) collision probability* for the set of events is

$$P_{agg}^{total} = P_{agg}(\mathcal{P}) = 1 - S_{agg}(\mathcal{P}) = 1 - \prod_{i=1}^N [1 - P_{c,i}] \quad (5)$$

The sequence of collision probabilities  $\mathcal{P}$  in (2) represents the associated values if the modeled mission performs no risk mitigation maneuvers, i.e., the unremediated risk. Next, consider a related sequence of *remediated* collision probabilities

$$\mathcal{P}_{rem} = P_{c,i}^{rem}, \quad i = 1, \dots, N, \quad (6)$$

that has been computed according to a risk mitigation strategy where a maneuver is performed whenever there is a value  $P_{c,i} > P_m$ , where  $P_m$  is the threshold which mandates a risk mitigation maneuver be performed whenever  $P_{c,i}$  exceeds its value. Often,  $P_m$  is referred to as either *the red threshold* or the *RMM threshold*. The corresponding remediated aggregate collision probability (which we refer to as *residual risk*) is then

$$P_{c,agg}^{rem} = P_{agg}(\mathcal{P}_{rem}) = 1 - \prod_{i=1}^N [1 - P_{c,i}^{rem}]. \quad (7)$$

Operationally, SpaceNav's maneuver planning service reduces the aggregate collision probability for a high  $P_c$  event to be below the value of  $10^{-7}$ , where the aggregate  $P_c$  is computed for all conjunction events over a time horizon around the TCA of the high  $P_c$  event. Typically, the time horizon is 3 days so that all conjunction events within 3 days of the high  $P_c$  event's TCA are considered in the aggregate collision probability calculation used in the maneuver planning process. In this analysis, we model residual risk in a manner which mimics SpaceNav's maneuver planning capabilities by considering 31 values for the RMM threshold  $P_m \in [10^{-6}, 10^{-3}]$  and 31 values of a *risk reduction factor* defined as  $\rho \in [10^{-3}, 1]$ . We assume that when an RMM is performed, the remaining aggregate probability of collision over a time horizon of 3 days is equal to the quantity  $\rho P_m$ . Table 2 describes this approach for risk remediation using some example values with a 3-day time horizon,  $\rho = 10^{-3}$ , and  $P_m = 10^{-4}$ , which simulate what is performed operationally by SpaceNav. In the results presented in §4, we also considered an alternative strategy where an RMM decision was made whenever the aggregate  $P_c$  value over the time horizon was greater than  $P_m$ , as opposed to triggering RMMs based on a single value of  $P_c$  alone. However, this alternative strategy did not appreciably change the overall results presented in this work and are not included.

It follows that, the average rate that a mission performs maneuvers according to this formulation is

$$\dot{N}_{RMM} = \frac{\left[ \sum_{i=1}^N U(P_{c,i} - P_m) \right]}{T}, \quad (8)$$

measured in risk mitigation maneuvers per-year, where  $U(x)$  denotes the unit step function

$$U(x) = \begin{cases} 0 & \text{for } x \leq 0 \\ 1 & \text{for } x > 0 \end{cases}. \quad (9)$$

3 Day Time Horizon For Day $j$															
$i$	1	2	3	4	5	6	7	8	9	10	11	12	13	14	15
Day #	j-1	j	j	j	j	j+1	j+1	j+1	j+2	j+2	j+2	j+2	j+3	j+3	j+3
$P_{c,i}$	0	0	0	2e-4	0	0	1e-12	0	0	0	0	3e-6	0	0	2e-11
$P_{c,i}^{rem}$	0	$\rho P_m$	0	0	0	0	0	0	0	0	0	0	0	0	2e-11

$\underbrace{\hspace{10em}}_{1e-7}$        $\uparrow$   $P_{c,i} > P_m$

Table 2: Example of a sequence of unremediated collision probabilities  $\{P_{c,i}\}_{i=1}^N$  as in (2), and the corresponding sequence of remediated collision probabilities  $\{P_{c,i}^{rem}\}_{i=1}^N$  as in (6). This example assumes  $\rho = 10^{-3}$ ,  $P_m = 10^{-4}$ , and a time horizon of 3 days. This visualization depicts our model for estimating residual risk where a single high  $P_c$  event triggers an RMM on day  $j$  and all events over the time horizon around the high  $P_c$  event, days  $j+1$  and  $j+2$ , are remediated so that their aggregate  $P_c$  value is  $\rho P_m$ . In this example considering 15  $P_c$  values, the unremediated risk is  $P_{agg}^{total} = 2.02999 \times 10^{-4}$  and the residual risk is  $P_{agg}^{rem} = 1.00020 \times 10^{-7}$ .

In order to better understand the residual risk in (7), we first introduce the notation and concepts originally presented in [15]. The total annual collision probability for a space vehicle is the sum of the fluxes of the individual conjuncting objects, multiplied by the area of the vehicle. Mathematically, this concept is represented by defining the total annual collision probability

$$P_T = \sum_j F_j A_{\otimes} = \sum_j \int_{A=0}^{\infty} P F_j dA, \quad (10)$$

which is the integral to infinity of the collision probability per unit area associated with constant collision probability contours within the conjunction plane. In (10),  $A_{\otimes}$  is the area of the target sphere typically defined by the sum of the primary and secondary hard body diameters, and  $F_j$  is the annual flux for the  $j^{\text{th}}$  object. Let  $A(P_m)$  be the area of the ellipse in the conjunction plane corresponding to values of  $P_c > P_m$ , then (10) can be expanded as

$$P_T = \sum_j \int_{A=0}^{A(P_m)} P F_j dA + \sum_j \int_{A(P_m)}^{\infty} P F_j dA = Q + R, \quad (11)$$

where  $Q$  is the risk reduction and  $R$  is the residual risk. From this formulation it is clear that risk reduction is defined such that all events corresponding to the area  $A(P_m)$  are considered completely mitigated by avoidance maneuvers. Such an assumption was used in [16], where it was assumed that a maneuver eliminates the risk for the conjunction for which it was made, and that no matter how many maneuvers are performed, risk from tracked debris is never eliminated, which is consistent with (11). For context, this type of residual risk estimation has been used in a variety of works, see [12, 13, 14, 15, 16, 23]. These works largely rely on the Kessler flux model formulation [22].

While the formulation for calculating  $P_c$  and debris flux is an intricate and complex issue, it is clear that risk reduction is defined in a conceptually simple manner. Specifically, the risk reduction is quantified as the risk (in terms of collision probability) that is removed by RMMs, see (11), and that the residual risk represents all remaining collision probability. While the previous works [12, 13, 14, 15, 16, 23] rely heavily on debris flux models in order to estimate risk reduction and residual risk, the high-level concepts may be adapted to the survival probability analysis framework described above. Consider that  $\mathcal{P}_{rem}$  as in (6) defines the sequence of collision probabilities corresponding to all unremediated events, as well as the remediated collision probabilities following avoidance maneuvers. Further, consider that the sequence of collision probabilities in  $\mathcal{P}$  as defined in (2) represents the total unremediated set of collision probabilities. From these definitions, we can define an alternative empirical, *aggregate risk reduction* as

$$P_{c,agg}^{pred} = P_{c,agg}^{total} - P_{c,agg}^{rem}. \quad (12)$$

Rearranging (12) yields another formulation of the total aggregate collision probability in (5) as

$$P_{c,agg}^{total} = P_{c,agg}^{pred} + P_{c,agg}^{rem}, \quad (13)$$

which is similar to (11). We define the *empirical risk reduction* to be  $P_{c,agg}^{pred}$ , and the *empirical residual risk* as  $P_{c,agg}^{rem}$ . In our analysis, when we refer to risk reduction and residual risk we specifically mean  $P_{c,agg}^{pred}$  and  $P_{c,agg}^{rem}$ , respectively.

This proposed formulation in (13) for residual risk has a few advantages compared to the traditional approach in (11). First, because the proposed strategy follows the semi-empirical method introduced in [18], it does not rely on a debris flux model to estimate risk, risk reduction, residual risk, or maneuver rates, but instead can be adapted to a sequence of collision probabilities which model or correspond to real operational events. Second, the proposed strategy allows us to model realistic risk reduction due to avoidance maneuvers through the risk reduction factor  $\rho$ . In this manner, we do not have to assume that the  $P_c$  is completely eliminated for a conjunction event which triggers an avoidance maneuver, as was the case in [16]. And third, this proposed strategy is empirical by design, so that it may be applied to historical conjunction data or to the simulated conjunction events resulting from a numerical simulation.

A topic we do not specifically consider but is adaptable to our proposed framework is the concept of “ducking” maneuvers. Ducking is an operational technique in which satellites may retract their solar panels and/or make attitude adjustments to assume a flat shape, thus reducing the surface area in the conjunction plane. These types of maneuvers are reported to reduce collision probability by 4 to 10 times [33], and could be represented in our model of residual risk through the risk reduction factor  $\rho$ .

Another topic we do not specifically address but has been studied is the notion of *consequence*, which is a function of the combined mass of two conjuncting objects, which is a proxy for the amount of debris likely produced if a collision were to occur [32]. Analysis in this field suggests that not all collisions in LEO are equal in terms of risk to the space environment, but instead among the most risky are potential collisions involving a massive intact derelict object, e.g., defunct payloads or abandoned rocket bodies [27].

### 3. RESIDUAL RISK AS A FUNCTION OF CONSTELLATION RISK AND SIZE

In this section, we present a mathematical formulation for calculating the necessary residual risk, per-year, per-satellite required for constellation of size  $N$  to have a target, aggregate, total risk below a specified value.

**Theorem 3.1.** *Let  $N$  be the number of satellites in a constellation,  $P_c^{total}$  be the target total risk for an entire constellation [ $y^{-1}$ ], and  $P_{c,agg}^{rem}$  be the aggregate remediated residual risk per-satellite [ $y^{-1}$ ], then the maximum residual risk per-satellite, per-year as a function of  $N$  and  $P_c^{total}$  is*

$$P_{c,agg}^{rem} = f(N, P_c^{total}) = 1 - (1 - P_c^{total})^{1/N}. \quad (14)$$

*Proof.* The target total risk for a constellation of size  $N$  given  $P_{c,agg}^{rem}$  is

$$P_c^{total} = 1 - \prod_{c=1}^N (1 - P_{c,agg}^{rem}). \quad (15)$$

Rearranging (15) and using the logarithm function yields

$$\Leftrightarrow \log \left( \prod_{c=1}^N [1 - P_{c,agg}^{rem}] \right) = \log (1 - P_c^{total}) \quad (16)$$

$$\Leftrightarrow \sum_{c=1}^N \left[ \log (1 - P_{c,agg}^{rem}) \right] = \log (1 - P_c^{total}) \quad (17)$$

$$\Leftrightarrow N \log (1 - P_{c,agg}^{rem}) = \log (1 - P_c^{total}) \quad (18)$$

$$\Leftrightarrow P_{c,agg}^{rem} = 1 - (1 - P_c^{total})^{1/N}, \quad (19)$$

which defines (14). □

Eq. (14) provides a way to estimate  $P_{c,agg}^{rem} = f(N, P_c^{total})$  as a function of constellation size and a desired value of  $P_c^{total}$ . Fig. 1 depicts the required residual risk per-satellite, per-year to achieve  $P_c^{total} \in \{10^{-1}, 10^{-2}, 10^{-3}, 10^{-4}, 10^{-5}\}$  for a constellation of size  $N = 1, \dots, 10000$ .

To understand these results, we consider the different configurations of satellite constellations for a given yearly, per-satellite residual risk. Consider  $P_{c,agg}^{rem} = 10^{-4}$ , this value corresponds to the following: a single satellite with yearly residual risk equal to  $10^{-4}$ , a constellation of 10 satellites with yearly  $P_c^{total} = 10^{-3}$ , a constellation of 100 satellites with yearly  $P_c^{total} = 10^{-2}$ , or a constellation of 1000 satellites with yearly  $P_c^{total} = 10^{-1}$ . Now consider a more ambitious risk posture of  $P_{c,agg}^{rem} = 10^{-5}$ , this value corresponds to the following: a single satellite with yearly residual risk equal to  $10^{-5}$ , a constellation of 10 satellites with yearly  $P_c^{total} = 10^{-4}$ , a constellation of 100 satellites with yearly  $P_c^{total} = 10^{-3}$ , a constellation of 1000 satellites with yearly  $P_c^{total} = 10^{-2}$ , or a constellation of 10 000 satellites with yearly  $P_c^{total} = 10^{-1}$ . As we demonstrate in §4, from an operational perspective, a target of  $P_{c,agg}^{rem} = 10^{-5}$  requires relatively conservative values of  $P_m$  and  $\rho$ , see Tables 6 and 8. Therefore, even assuming relatively conservative values of  $P_m$  and  $\rho$  to achieve  $P_{c,agg}^{rem} = 10^{-5}$ , we highlight the fact that  $P_c^{total} = 10^{-1}$  is remarkably large when considering large constellations of satellites, e.g.,  $N = 10000$ .

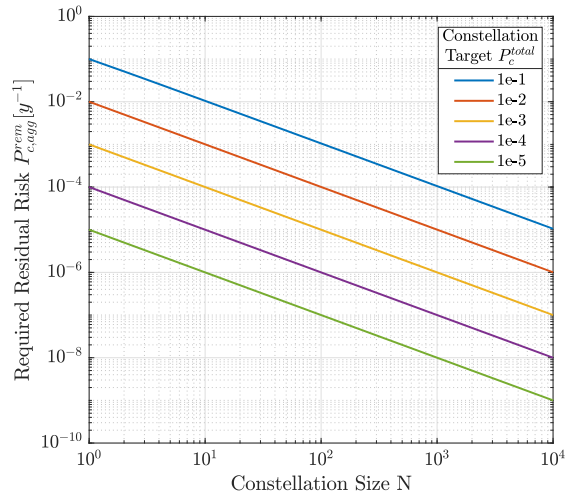


Fig. 1: Required average residual risk per-satellite, per-year to achieve  $P_c^{total}$  for a constellation of size  $N$  as in (14).

## 4. RESULTS

This section documents the numerical results obtained by SpaceNav’s CAS for AQUA and ICESat-2.

Each primary satellite was simulated using a constellation shell containing  $N_p = 50$  orbital planes, with  $N_{spp} = 50$  satellites per plane. The orbital planes of the shell are uniformly spaced in RAAN, and the satellites in each plane are uniformly spaced in true anomaly. The simulation time span covers 3 days beginning on 2022-04-23. The simulation resulted in 55 354 total conjunction events for the AQUA constellation, and 59 159 events for the ICESat-2 constellation. AQUA conjunctions which corresponded to A-train or C-train satellites were removed by their NORAD CAT IDs. This is done to remove model bias which would occur when the different orbital planes of the constellation shell interact with the historical orbital plane of the A-train and C-train satellites. Because these satellites all orbit Earth in the same orbital plane and are separated so that their relative positions remain approximately constant, we do not wish to simulate conjunction events between AQUA and itself, or any of these other satellites. Similarly, ICESat-2 conjunctions corresponding to ICESat-2 itself were also removed. Upon removing the conjunction events corresponding to the simulated shell and A-train and C-train satellites and removing ICESat-2’s conjunctions with itself, there were 53 065 simulated conjunction events for AQUA, and 58 519 events for ICESat-2. For AQUA, 1726 events were with analyst objects (with  $80000 \leq \text{NORAD CAT ID} \leq 99999$ ) and the total number of unique secondary objects encountered was 2432. For ICESat-2, 168 events were with analyst objects and the total number of unique secondary objects encountered was 1205. Fig. 2 depicts the secondary object type distributions for AQUA and ICESat-2 resulting from the CAS numerical simulation.

### 4.1 Event Frequency

For each primary satellite, the number of conjunction events per day was computed for each day of the simulation. These computed values were used form empirical distributions of event frequency. The event frequency distributions presented here were used in the computation of collision probability and maneuver frequency described in §2.6. Figures 3a and 4a show the distributions of the number of events per day per satellite for simulated conjunction events. The statistics of the number of events per day per satellite are summarized in Tables 3b and 4b.

Fig. 5 depicts the estimate of average conjunction event frequency as a function of simulation propagation time and provides evidence that the CAS simulation was run with sufficient exposure time to obtain a good estimate of the event frequency distributions.

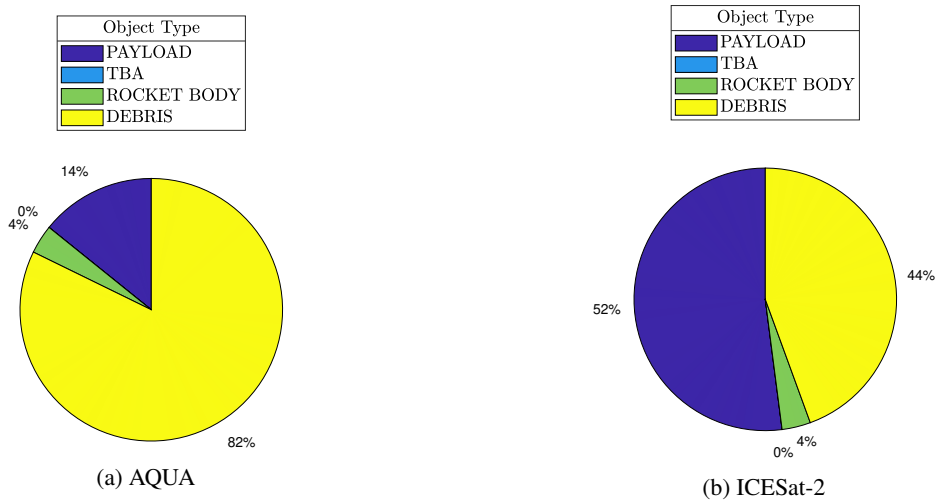
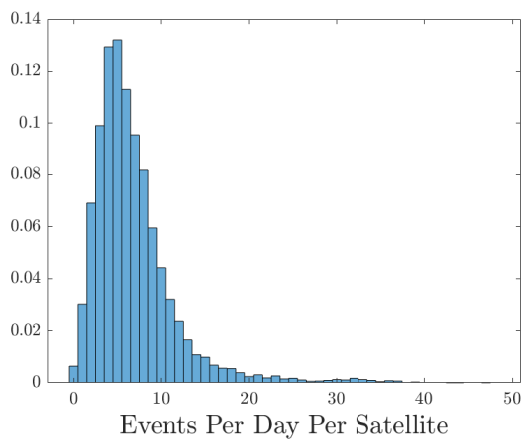


Fig. 2: Simulated Secondary Object Type Distributions for AQUA and ICESat-2.

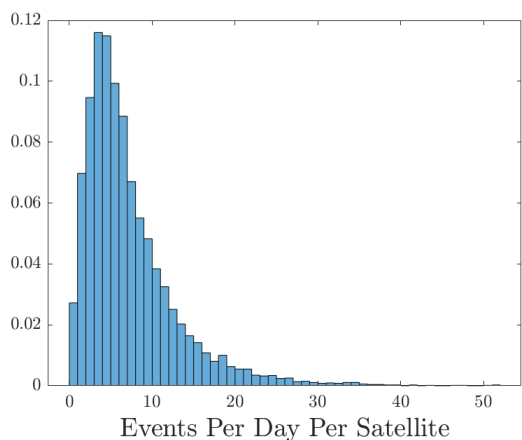


(a)

Statistic	Value	95 % C.I.
Minimum	0	
Maximum	48	
Median	6	
Mode	5	
Mean	6.84	[6.71141, 6.98531]
Std. Dev.	4.87127	[4.62547, 5.1496]

(b)

Fig. 3: Per-satellite estimated event frequency distribution and statistics for AQUA shown in 3a and 3b, respectively.



(a)

Statistic	Value	95 % C.I.
Minimum	0	
Maximum	52	
Median	5	
Mode	3	
Mean	6.7504	[6.59829, 6.91764]
Std. Dev.	5.63165	[5.42762, 5.87635]

(b)

Fig. 4: Per-satellite estimated event frequency distribution and statistics for ICESat-2 shown in 4a and 4b, respectively.

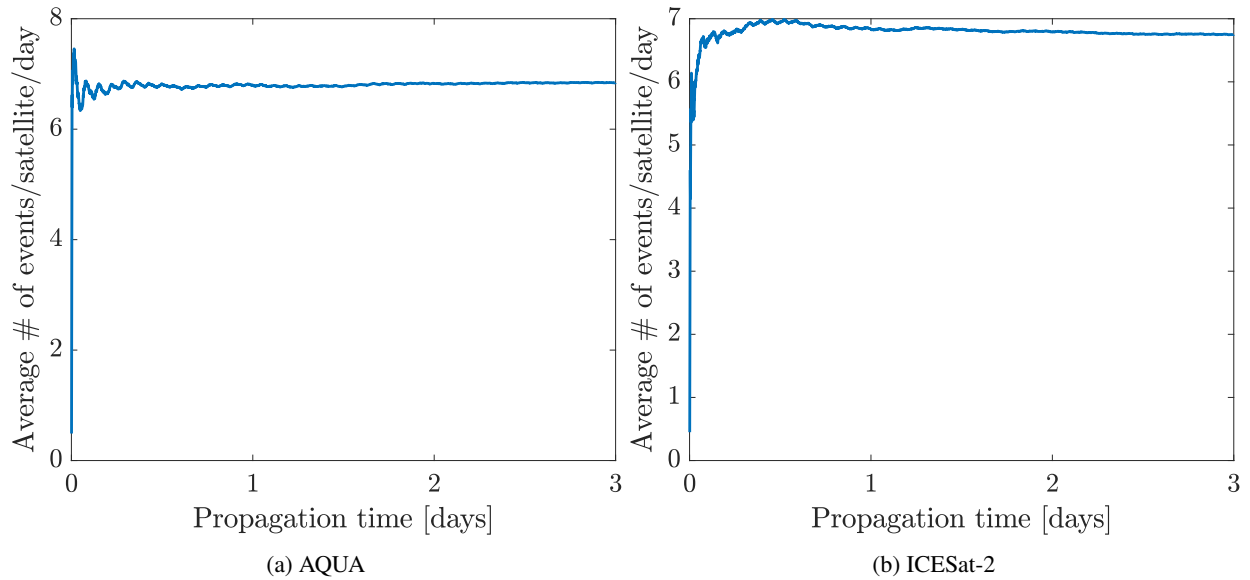


Fig. 5: Convergence of average maneuver frequency estimates for AQUA and ICESat-2.

## 4.2 RIC Distributions

The RIC miss geometry distributions resulting from all simulated conjunction events are summarized in Fig. 6. Note that these RIC distributions were used in the computation of collision probability described in §2.6. As previously mentioned, the numerical simulations presented in this work have been validated to achieve sufficient exposure time by measuring Monte Carlo convergence of event frequency and the differences in the RIC miss distributions with respect to propagation time. However, we do not include convergence analysis regarding the RIC relative position component distributions as it is not the main focus of this work.

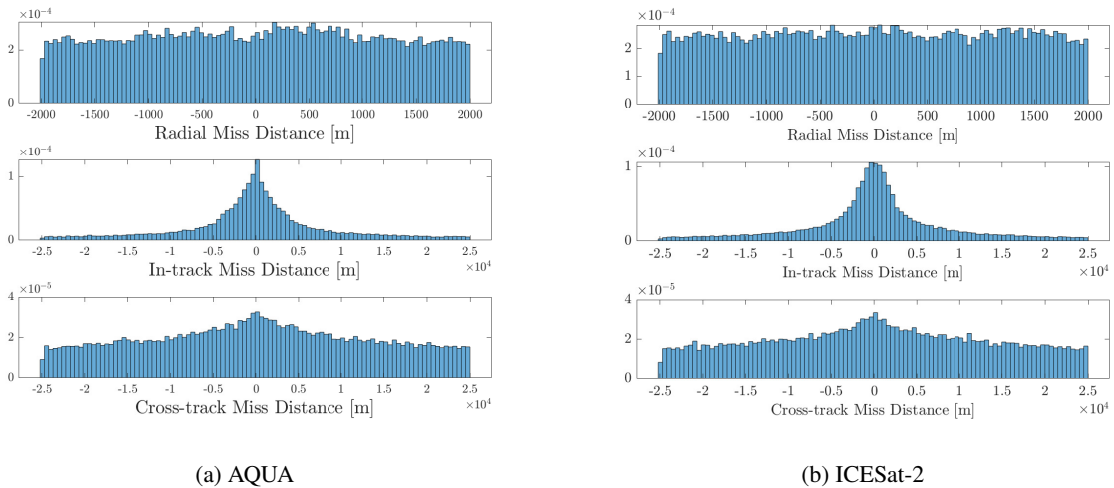


Fig. 6: RIC miss geometry distributions for AQUA and ICESat-2.

## 4.3 Covariance Generation

Position uncertainty in the form of RIC covariance is known to be dominated by propagation time,  $\Delta t_{TCA}$ . To form representative covariance data sets which enable computation of  $P_c$ , we employed historical CDM data with TCAs ranging from 2021-01-01 to 2022-06-15, see Tables 3 and 4. These historical events contain covariance data corresponding

to precision orbits built by the 18<sup>th</sup> SDS<sup>1</sup> and therefore form a data set of realistic covariances for the primaries and the secondary object population, as seen in an operational environment. Figures 7 and 8 depict the secondary object covariances summarized with empirical cumulative distribution functions of the RIC position standard deviations. Primary covariance distributions are also generated from the CDMs, but figures describing them are not included in this analysis for brevity and due to the fact that secondary uncertainty dominates  $P_c$  computations relative to primary uncertainty. These figures demonstrate that there are significant correlations in position uncertainty distributions with respect to  $\Delta t_{TCA}$ , as expected. This effect is more pronounced in the in-track uncertainty compared to the radial and cross-track uncertainties. Although we do not present the distributions of the off-diagonal covariance terms, they are accounted for in the computation of  $P_c$ .

Table 3: Summary of historical AQUA CDM data set by propagation time  $\Delta t_{TCA}$ .

Bin Number	1	2	3	4	5	6
Propagation Time Range, $\Delta t_{TCA}$ [hours]	[0, 4)	[4, 8)	[8, 12)	[12, 16)	[16, 20)	[20, 24)
Number of CDMs	190	865	1274	1453	1602	1648

Table 4: Summary of historical ICESat-2 CDM data set by propagation time  $\Delta t_{TCA}$ .

Bin Number	1	2	3	4	5	6
Propagation Time Range, $\Delta t_{TCA}$ [hours]	[0, 4)	[4, 8)	[8, 12)	[12, 16)	[16, 20)	[20, 24)
Number of CDMs	213	1286	1722	2032	2123	2076

#### 4.4 Collision Probability, Maneuver Statistics, and Residual Risk

In this section, we present the results following the collision probability and maneuver frequency estimation procedure defined in §2.6 and the residual risk estimation procedure defined in §2.7. This procedure uses the simulated event frequency distributions presented in Figures 3 and 4. This procedure also uses the relative position and velocity vectors for the primaries and secondaries summarized by the RIC miss geometry distributions in Fig. 6. Data-driven primary and secondary covariance values resulting from the historical data analysis presented in §4.3 are employed to facilitate  $P_c$  computations. Different maneuver execution times are simulated by using covariance values selected from 6 different propagation time bins, where propagation time  $\Delta t_{TCA}$  is defined as the TCA minus the last observation time. The  $\Delta t_{TCA}$  bins cover 0–4, 4–8, 8–12, 12–16, 16–20, and 20–24 hours. For collision probability computations, hard body radius (HBR) values used in  $P_c$  computations are dynamic based on object type. The following HBR values are assumed in this work: 5 m for payloads, 3 m for rocket bodies, and 1.5 m for debris and unknown objects. The primary HBR values were 15.8 m and 5.5 m for AQUA and ICESat-2, respectively. Every estimate of maneuver frequency and residual risk presented in this section is the average result of 2400 independently simulated years.

The results of the Monte Carlo simulation used to estimate maneuver frequency are presented in Fig. 9. Maneuver frequency, unlike residual risk, is independent of the risk reduction factor  $\rho$ . Generally, Fig. 9 indicates that smaller RMM thresholds result in more frequent RMMs while larger RMM thresholds correspond to fewer RMMs. Despite there being a higher overall density of objects near AQUA’s 700 km orbit compared to ICESat-2’s orbit at 480 km [4], and despite AQUA’s larger HBR, ICESat-2 has overall higher estimates of maneuver frequency. The larger values of ICESat-2’s maneuver frequency compared to AQUA’s are due to the generally larger covariance values (see §4.3), which can be attributed to the greater effects of atmospheric drag uncertainty at lower altitudes, and these larger covariance values result in more events where  $P_c > P_m$ . With the exception of AQUA using the 12–16 hour covariance bin and  $P_m = 10^{-6}$ , there is a majority of evidence showing that smaller maneuver execution times correspond to fewer required RMMs.

Fig. 10 depicts the results of the Monte Carlo simulation used to estimate yearly per-satellite residual risk,  $P_{c,agg}^{rem}$ . Unlike maneuver frequency, residual risk is dependent on  $\rho$ , therefore this figure only shows data for a fixed risk reduction factor  $\rho = 0.001$ . Fig. 10 shows that smaller maneuver execution times result in lower residual risk, and

<sup>1</sup>We do not include CDMs corresponding to owner/operator ephemerides.

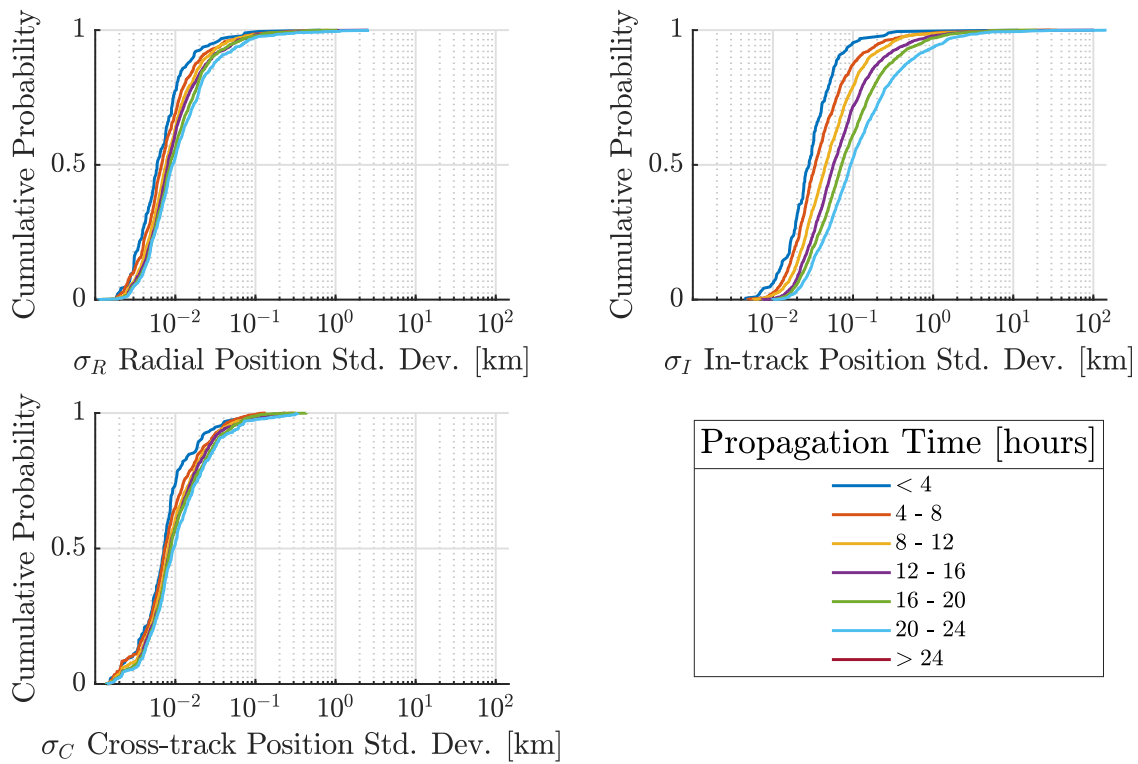


Fig. 7: AQUA secondary object RIC position standard deviation distributions by propagation time.

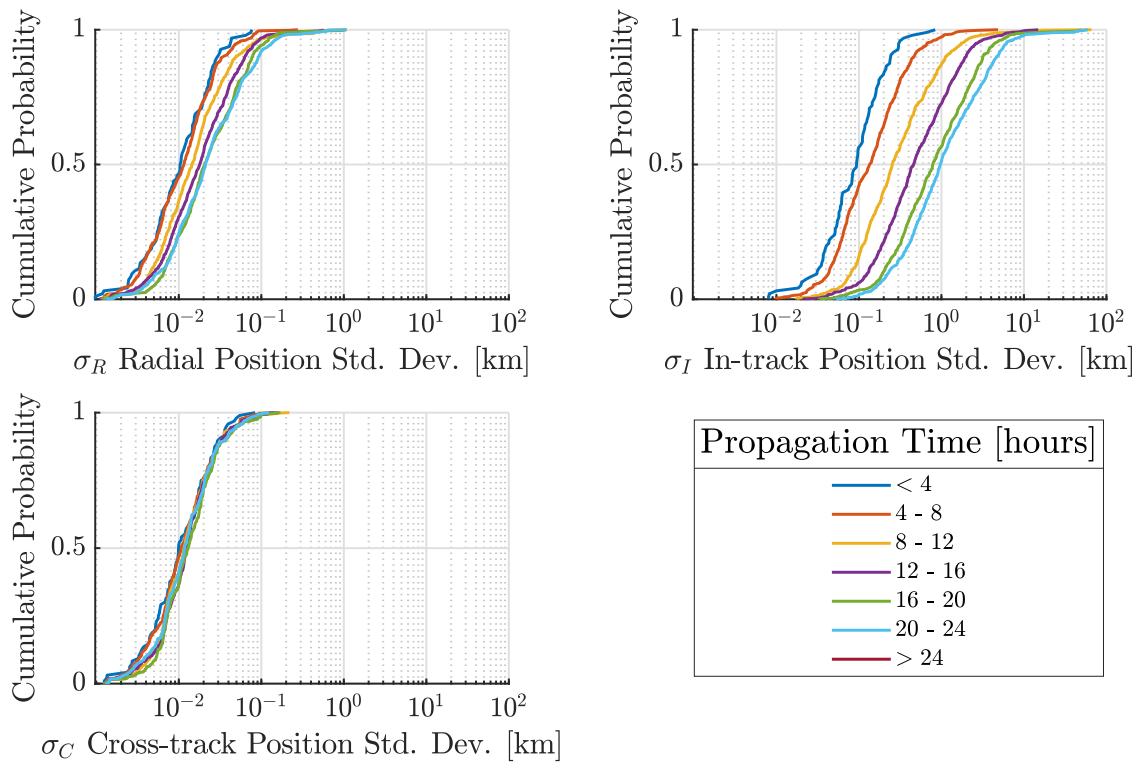


Fig. 8: ICESat-2 secondary object RIC position standard deviation distributions by propagation time.

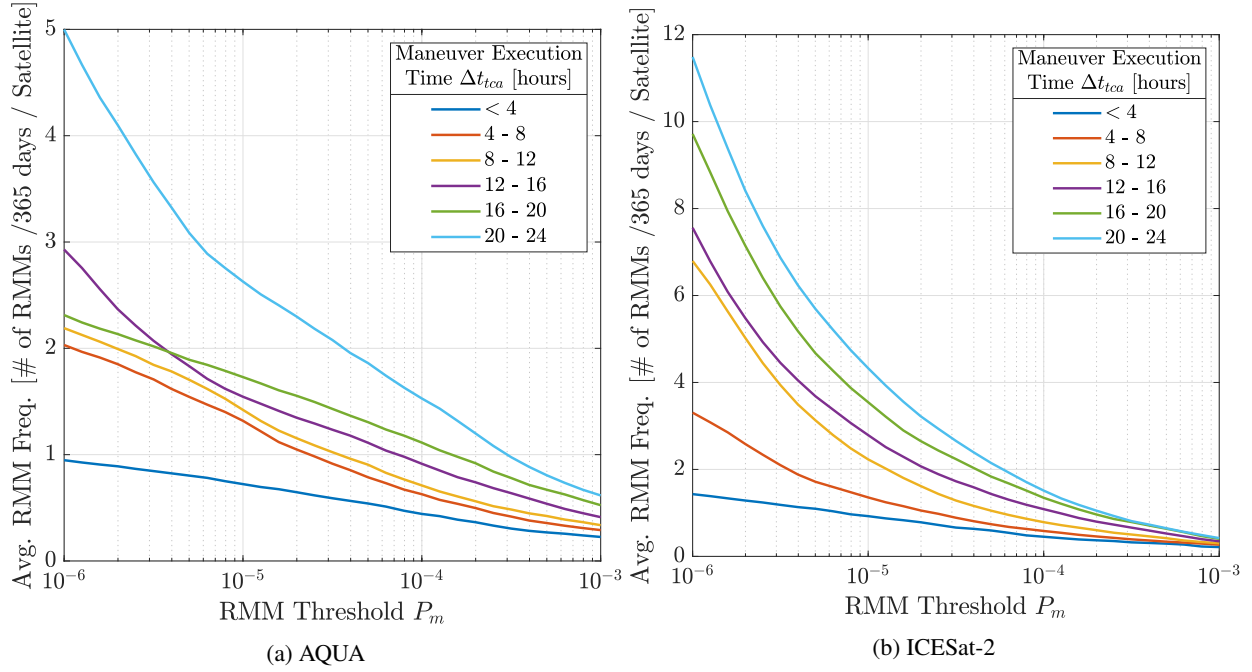


Fig. 9: Average, yearly per-satellite maneuver frequency as a function of RMM threshold  $P_m$ .

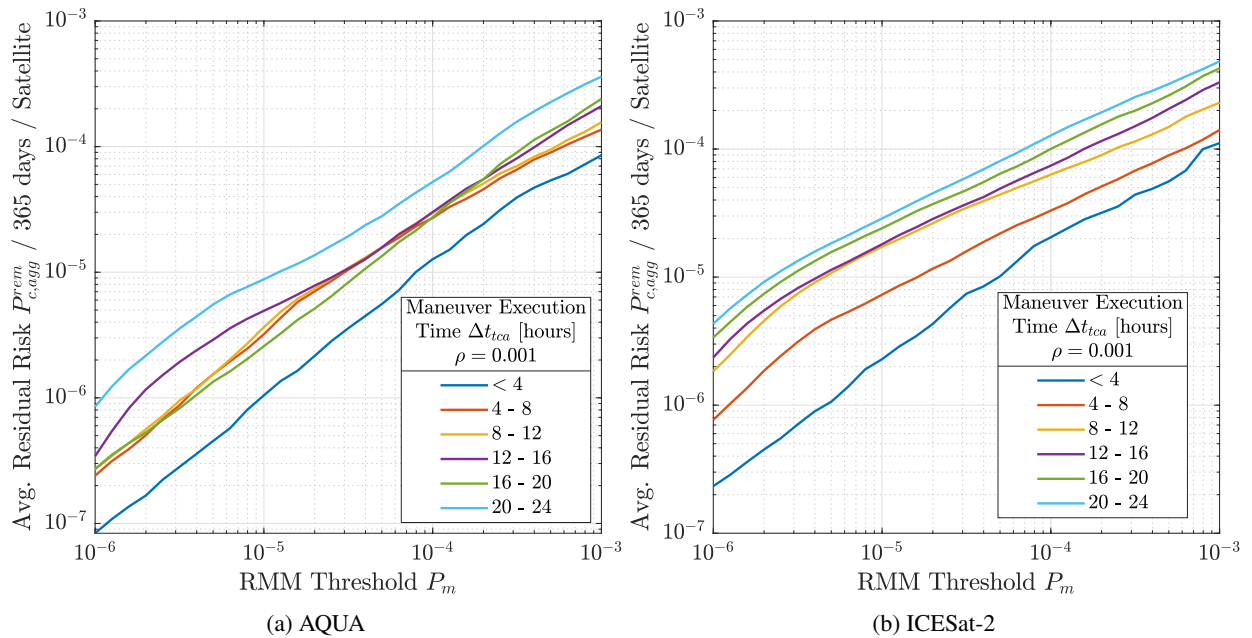


Fig. 10: Average, yearly per-satellite residual risk as a function of RMM threshold  $P_m$  for a fixed  $\rho = 0.001$ .

that lower RMM thresholds also result in lower residual risk. The overall values of  $P_{c,agg}^{rem}$  for ICESat-2 are larger than for AQUA, considering similar  $\Delta t_{TCA}$ ,  $\rho$ , and  $P_m$  values. This is due to the generally larger covariance values (see §4.3) for ICESat-2. For AQUA, almost all values of residual risk are such that  $P_{c,agg}^{rem} < P_m$ , while the same is not true for ICESat-2 where many values of  $P_{c,agg}^{rem} > P_m$ , particularly for  $\Delta t_{TCA} > 8$  hours and  $P_m < 10^{-5}$ . In general, these results show that the difference between residual risk and the RMM threshold is generally not more than one order of magnitude when considering  $\rho = 0.001$ .

To get a broader view of how changing  $P_m$ ,  $\rho$ , and  $\Delta t_{TCA}$  affects residual risk we estimated values of  $P_{c,agg}^{rem}$  for 31 values of  $\rho \in [10^{-3}, 1]$  and 31 values of  $P_m \in [10^{-6}, 10^{-3}]$ . Figures 11 through 16 depict contour plots of  $P_{c,agg}^{rem}$  as a function of  $P_m$  and  $\rho$  for each maneuver execution time bin considered. These contour plots summarize a sensitivity analysis of residual risk with respect to the RMM threshold, risk reduction factor, and the maneuver execution time, and demonstrate that each of these parameters—which together make up a risk mitigation strategy—have a significant role in determining residual risk. As expected, smaller values of the risk reduction factor  $\rho$  correspond to smaller values of  $P_{c,agg}^{rem}$ . Smaller  $\Delta t_{TCA}$  values and smaller values of  $P_m$  correspond to smaller values of  $P_{c,agg}^{rem}$ , as in Fig. 10, which represents the data on the left side of each contour plot where  $\rho = 0.001$ .

These contour plots indicate there are multiple configurations of  $P_m$ ,  $\rho$ , and  $\Delta t_{TCA}$  for which a satellite could achieve a target residual risk value  $P_{c,agg}^{rem}$ . For example, consider ways in which AQUA could achieve  $P_{c,agg}^{rem} = 10^{-5}$  for  $\Delta t_{TCA} < 4$  hours. According to Fig. 11a, there exists a contour of constant  $P_{c,agg}^{rem} = 10^{-5}$  which occurs for a variety of RMM threshold and risk reduction factor pairs, with one extreme occurring when  $(P_m, \rho) = (7.9432 \times 10^{-4}, 10^{-3})$  and the other when  $(P_m, \rho) = (1.25893 \times 10^{-5}, 1)$ .

From this analysis, it is clear that to achieve a desired residual risk using a relatively large RMM threshold and a small risk reduction factor is equivalent in terms of residual risk to using a small RMM threshold and a large risk reduction factor. These two extremes would result in fundamentally different risk mitigation strategies. In the first case, the operator would be opting to maneuver less frequently but mitigate risk for high  $P_c$  events considerably, and in the second case the operator would be opting to maneuver more frequently but mitigate less risk for high  $P_c$  events. One strategy or the other might be better suited to a particular mission. For example, due to engineering design constraints it might be more economical to perform more frequent small maneuvers versus a few large maneuvers, as might be the case for a satellite in a constellation. Or perhaps due to strict operational or station keeping constraints, executing RMMs might want to be avoided as much as possible (such is the case for AQUA, which is an Earth-observing science mission), in which case fewer but larger maneuvers might be a more attractive option to the satellite operator.

This analysis also demonstrates that the maneuver execution time plays a significant role in determining residual risk. For spacecraft with better maneuver planning capabilities and resources, waiting until  $\Delta t_{TCA}$  is small, e.g.,  $\approx 4$  hours in the case of AQUA, is feasible and therefore larger values of  $P_m$  and  $\rho$  might be considered compared to spacecraft with lesser maneuver planning capabilities and resources. Because  $\Delta t_{TCA}$  is essentially a proxy for the magnitude of the covariance used in  $P_c$  computations, this also means that future innovations in space situational awareness such as enhanced maneuver planning capabilities, or improvements to object tracking and its frequency, as well as more constant ephemeris screening systems, could potentially lead to an overall reduction to residual risk and consequently risk to the space environment.

Table 5 shows the limiting values of  $P_m$  and  $\rho$ , for a fixed  $\Delta t_{TCA}$ , which correspond to constant contours of  $P_{c,agg}^{rem} = 10^{-4}$  for AQUA. Table 5 indicates that  $P_{c,agg}^{rem} = 10^{-4}$  is possible with values of  $P_m$  ranging from  $3.9 \times 10^{-5}$  to  $10^{-3}$  and with values of  $\rho$  ranging from  $10^{-3}$  to 1. Likewise, Table 6 shows the limiting values of  $P_m$  and  $\rho$ , for a fixed  $\Delta t_{TCA}$ , which correspond to constant contours of  $P_{c,agg}^{rem} = 10^{-5}$  for AQUA. Table 6 indicates that  $P_{c,agg}^{rem} = 10^{-5}$  is possible with values of  $P_m$  ranging from  $2 \times 10^{-6}$  to  $7.9 \times 10^{-5}$  and with values of  $\rho$  ranging from  $10^{-3}$  to 1.

Table 7 shows the limiting values of  $P_m$  and  $\rho$ , for a fixed  $\Delta t_{TCA}$ , which correspond to constant contours of  $P_{c,agg}^{rem} = 10^{-4}$  for ICESat-2. Table 7 indicates that  $P_{c,agg}^{rem} = 10^{-4}$  is possible with values of  $P_m$  ranging from  $1.7 \times 10^{-5}$  to  $8 \times 10^{-4}$  and with values of  $\rho$  ranging from  $10^{-3}$  to 1. Likewise, Table 8 shows the limiting values of  $P_m$  and  $\rho$ , for a fixed  $\Delta t_{TCA}$ , which correspond to constant contours of  $P_{c,agg}^{rem} = 10^{-5}$  for ICESat-2. Table 8 indicates that  $P_{c,agg}^{rem} = 10^{-5}$  is possible with values of  $P_m$  ranging from  $10^{-6}$  to  $5.0 \times 10^{-5}$  and with values of  $\rho$  ranging from  $10^{-3}$  to 1.

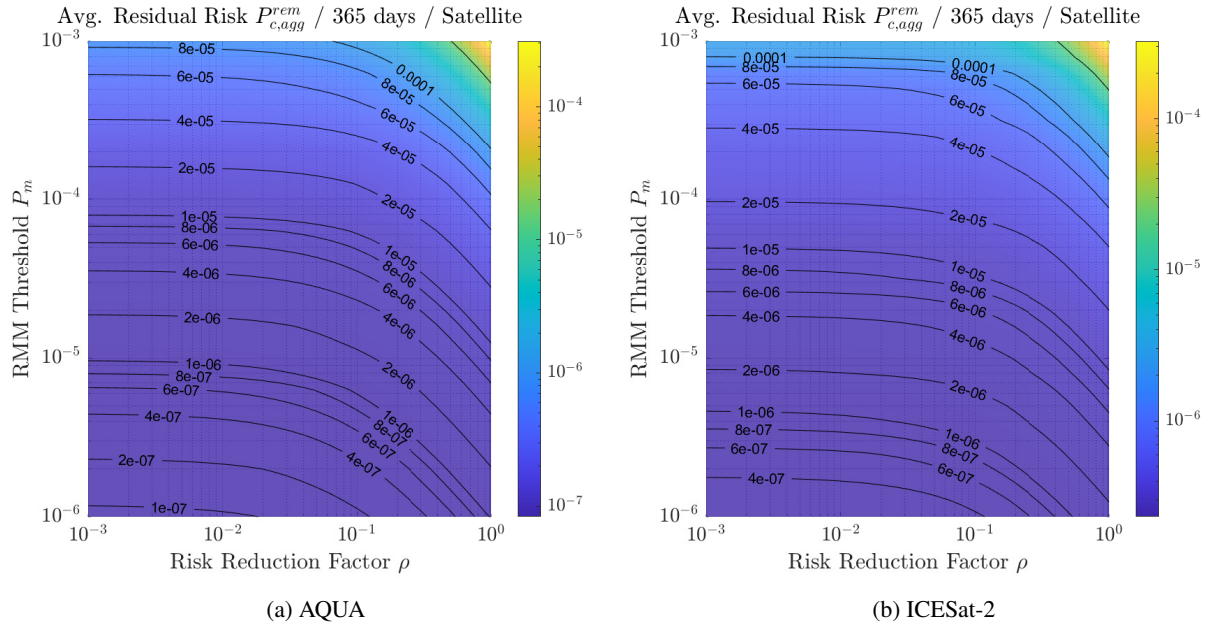


Fig. 11: **Maneuver execution time  $0 \leq \Delta t_{TCA} < 4$  hours**: average, yearly per-satellite residual risk  $P_{c,agg}^{rem}$  as a function of RMM threshold  $P_m$  and risk reduction factor  $\rho$ .

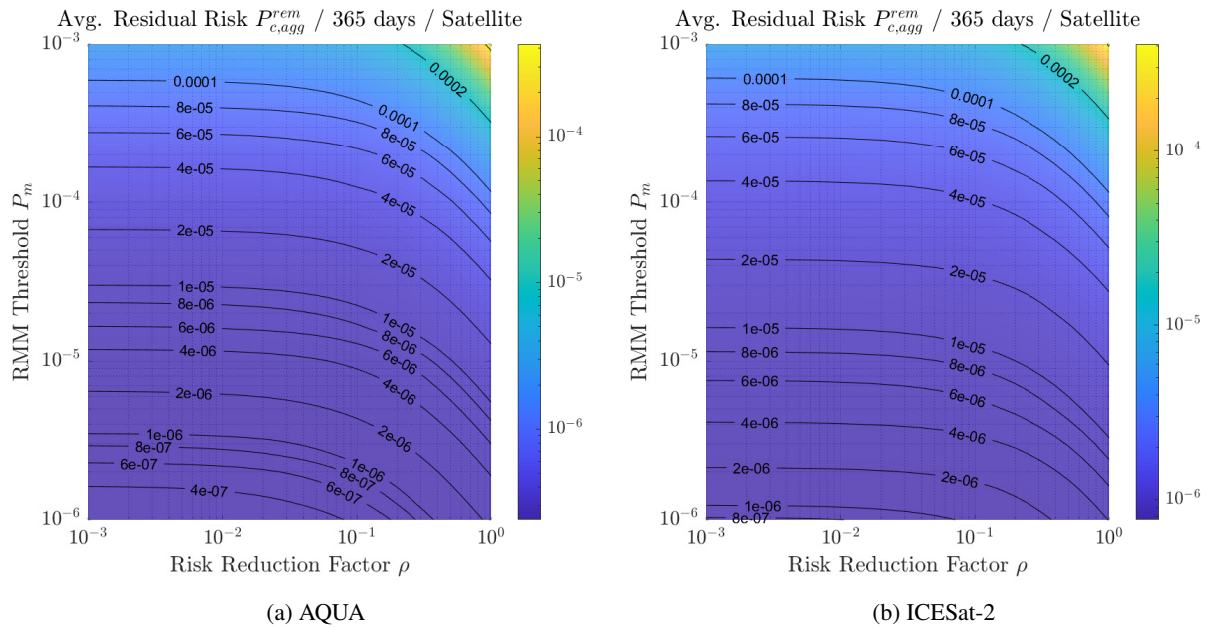


Fig. 12: **maneuver execution time  $4 \leq \Delta t_{TCA} < 8$  hours**: average, yearly per-satellite residual risk  $P_{c,agg}^{rem}$  as a function of RMM threshold  $P_m$  and risk reduction factor  $\rho$ .

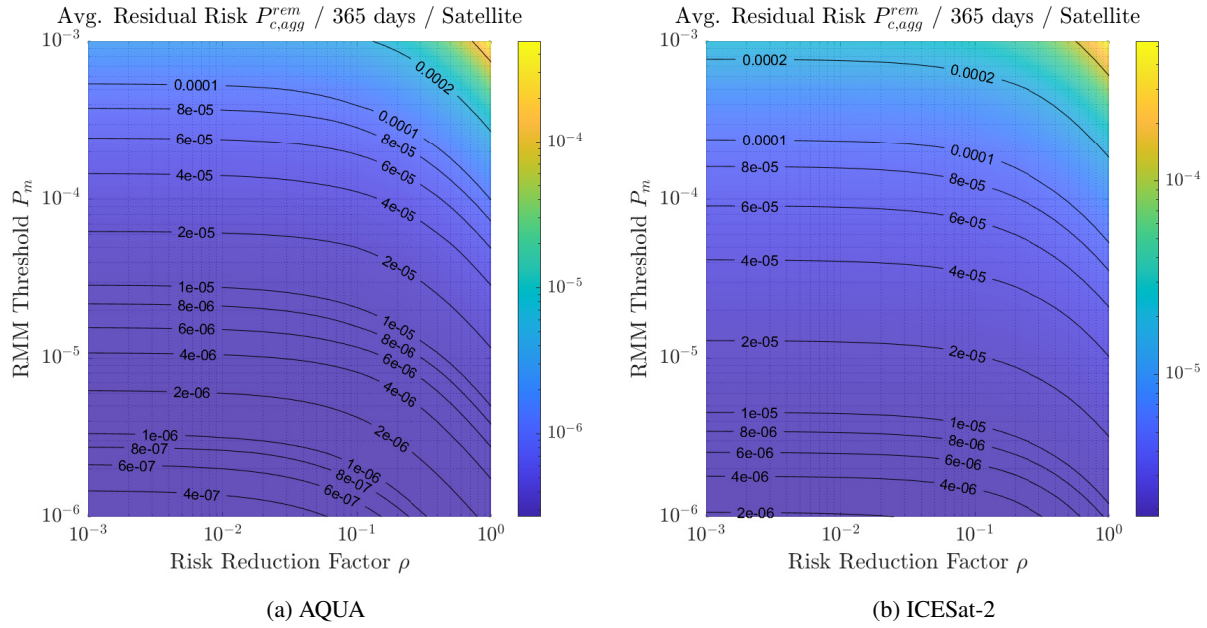


Fig. 13: **maneuver execution time  $8 \leq \Delta t_{TCA} < 12$  hours**: average, yearly per-satellite residual risk  $P_{c,agg}^{prem}$  as a function of RMM threshold  $P_m$  and risk reduction factor  $\rho$ .

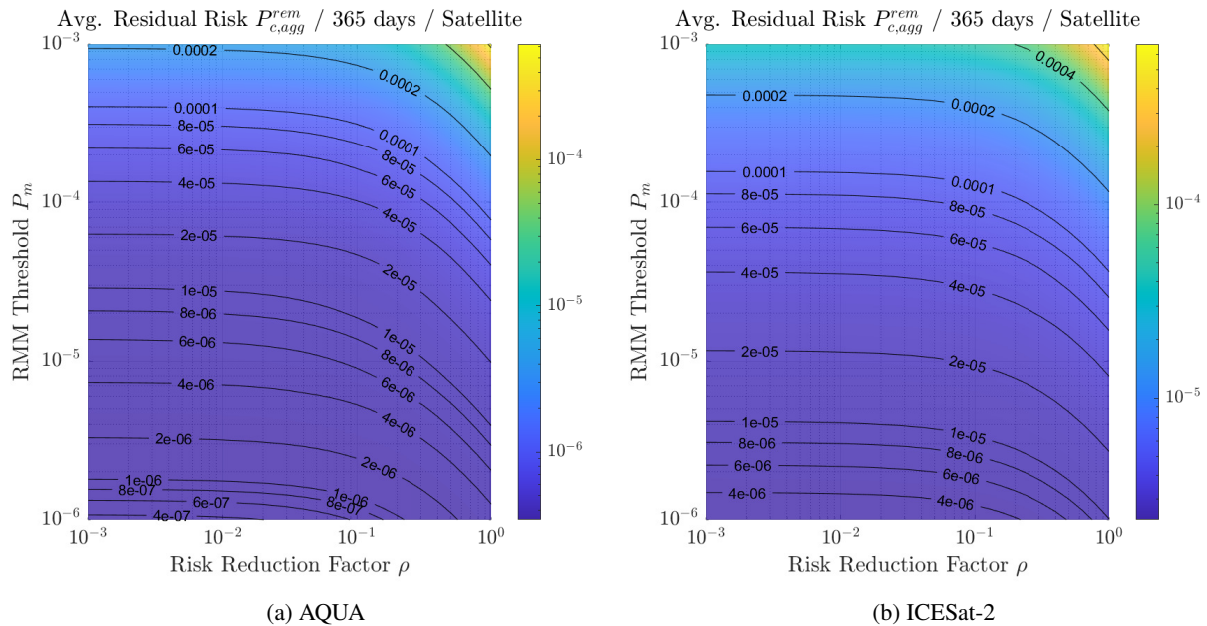


Fig. 14: **maneuver execution time  $12 \leq \Delta t_{TCA} < 16$  hours**: average, yearly per-satellite residual risk  $P_{c,agg}^{prem}$  as a function of RMM threshold  $P_m$  and risk reduction factor  $\rho$ .

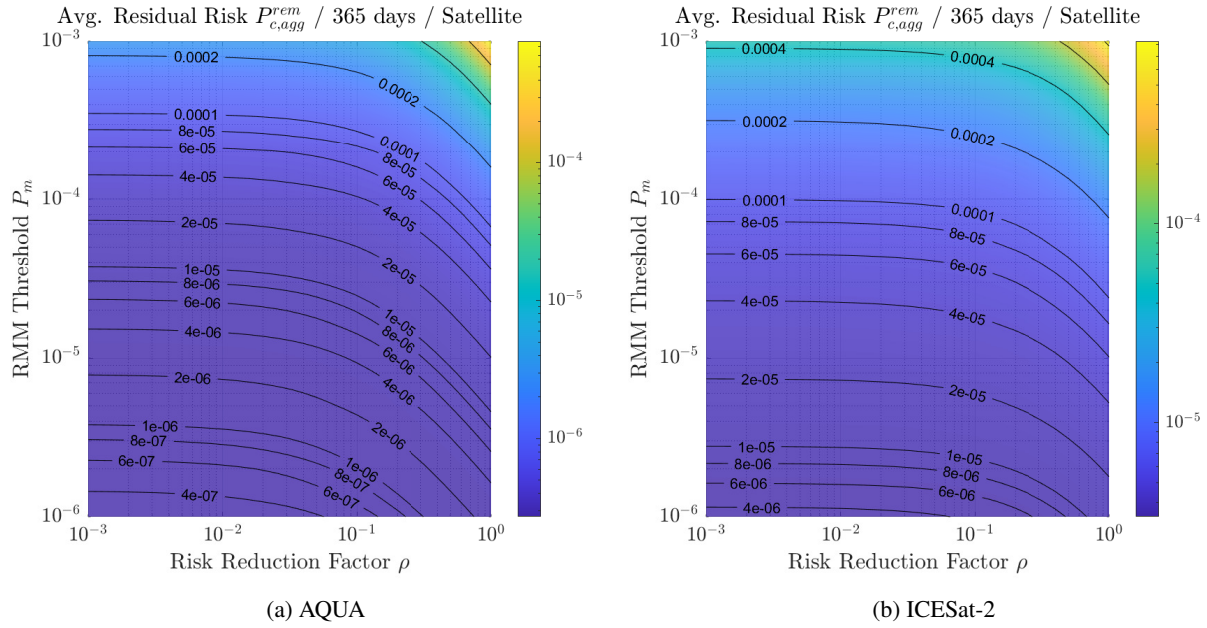


Fig. 15: **maneuver execution time  $16 \leq \Delta t_{TCA} < 20$  hours:** average, yearly per-satellite residual risk  $P_{c,agg}^{rem}$  as a function of RMM threshold  $P_m$  and risk reduction factor  $\rho$ .

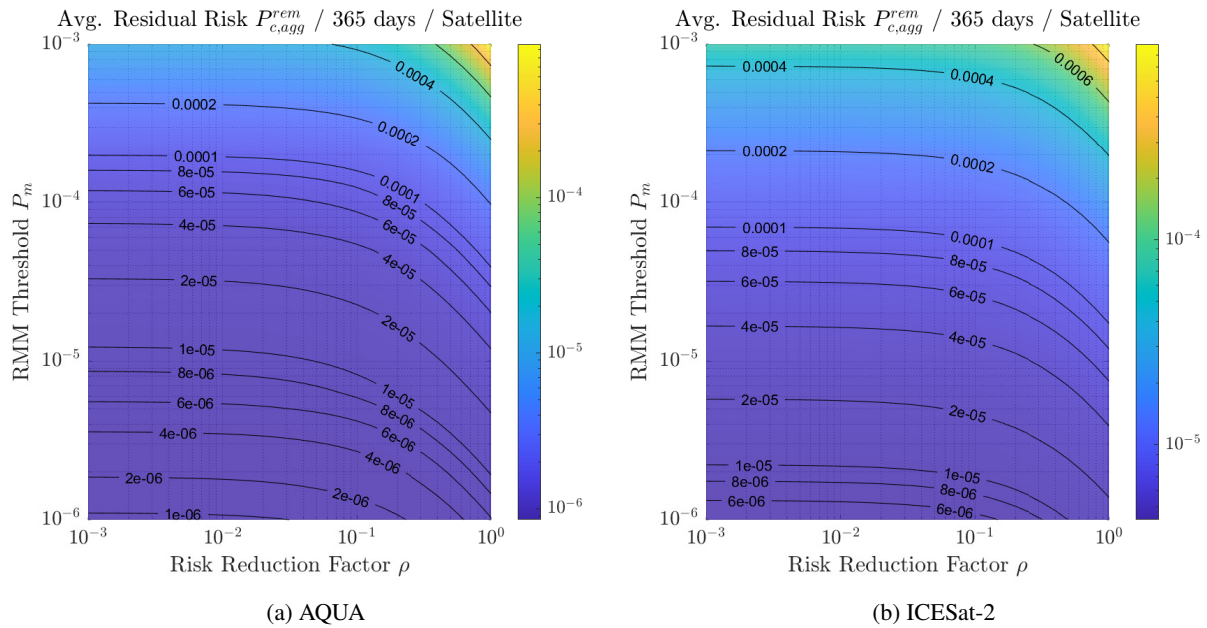


Fig. 16: **maneuver execution time  $20 \leq \Delta t_{TCA} < 24$  hours:** average, yearly per-satellite residual risk  $P_{c,agg}^{rem}$  as a function of RMM threshold  $P_m$  and risk reduction factor  $\rho$ .

Table 5: Range of  $(P_m, \rho)$  pairs yielding yearly, per-satellite residual risk  $P_{c,agg}^{rem} = 10^{-4}$  for AQUA.

$\Delta t_{TCA}$	(max $P_m$ , min $\rho$ )	(min $P_m$ , max $\rho$ )
$0 \leq \Delta t_{TCA} < 4$	$(1.0 \times 10^{-3}, 0.066)$	$(2.1 \times 10^{-4}, 1)$
$4 \leq \Delta t_{TCA} < 8$	$(5.9 \times 10^{-4}, 10^{-3})$	$(1.2 \times 10^{-4}, 1)$
$8 \leq \Delta t_{TCA} < 12$	$(5.4 \times 10^{-4}, 10^{-3})$	$(1.0 \times 10^{-4}, 1)$
$12 \leq \Delta t_{TCA} < 16$	$(4.1 \times 10^{-4}, 10^{-3})$	$(7.7 \times 10^{-5}, 1)$
$16 \leq \Delta t_{TCA} < 20$	$(3.5 \times 10^{-4}, 10^{-3})$	$(6.7 \times 10^{-5}, 1)$
$20 \leq \Delta t_{TCA} < 24$	$(2.0 \times 10^{-4}, 10^{-3})$	$(3.9 \times 10^{-5}, 1)$

Table 6: Range of  $(P_m, \rho)$  pairs yielding yearly, per-satellite residual risk  $P_{c,agg}^{rem} = 10^{-5}$  for AQUA.

$\Delta t_{TCA}$	(max $P_m$ , min $\rho$ )	(min $P_m$ , max $\rho$ )
$0 \leq \Delta t_{TCA} < 4$	$(7.9 \times 10^{-5}, 10^{-3})$	$(1.3 \times 10^{-5}, 1)$
$4 \leq \Delta t_{TCA} < 8$	$(3.0 \times 10^{-5}, 10^{-3})$	$(5.5 \times 10^{-6}, 1)$
$8 \leq \Delta t_{TCA} < 12$	$(2.9 \times 10^{-5}, 10^{-3})$	$(5.0 \times 10^{-6}, 1)$
$12 \leq \Delta t_{TCA} < 16$	$(2.9 \times 10^{-5}, 10^{-3})$	$(4.0 \times 10^{-6}, 1)$
$16 \leq \Delta t_{TCA} < 20$	$(3.8 \times 10^{-5}, 10^{-3})$	$(4.6 \times 10^{-6}, 1)$
$20 \leq \Delta t_{TCA} < 24$	$(1.3 \times 10^{-5}, 10^{-3})$	$(2.0 \times 10^{-6}, 1)$

Table 7: Range of  $(P_m, \rho)$  pairs yielding yearly per-satellite residual risk  $P_{c,agg}^{rem} = 10^{-4}$  for ICESat-2.

$\Delta t_{TCA}$	(max $P_m$ , min $\rho$ )	(min $P_m$ , max $\rho$ )
$0 \leq \Delta t_{TCA} < 4$	$(8.0 \times 10^{-4}, 10^{-3})$	$(1.9 \times 10^{-4}, 1)$
$4 \leq \Delta t_{TCA} < 8$	$(6.1 \times 10^{-4}, 10^{-3})$	$(1.2 \times 10^{-4}, 1)$
$8 \leq \Delta t_{TCA} < 12$	$(2.4 \times 10^{-4}, 10^{-3})$	$(5.3 \times 10^{-5}, 1)$
$12 \leq \Delta t_{TCA} < 16$	$(1.6 \times 10^{-4}, 10^{-3})$	$(3.7 \times 10^{-5}, 1)$
$16 \leq \Delta t_{TCA} < 20$	$(1.0 \times 10^{-4}, 10^{-3})$	$(2.4 \times 10^{-5}, 1)$
$20 \leq \Delta t_{TCA} < 24$	$(7.0 \times 10^{-5}, 10^{-3})$	$(1.7 \times 10^{-5}, 1)$

Table 8: Range of  $(P_m, \rho)$  pairs yielding yearly, per-satellite residual risk  $P_{c,agg}^{rem} = 10^{-5}$  for ICESat-2.

$\Delta t_{TCA}$	(max $P_m$ , min $\rho$ )	(min $P_m$ , max $\rho$ )
$0 \leq \Delta t_{TCA} < 4$	$(5.0 \times 10^{-5}, 10^{-3})$	$(8.0 \times 10^{-6}, 1)$
$4 \leq \Delta t_{TCA} < 8$	$(1.6 \times 10^{-5}, 10^{-3})$	$(3.3 \times 10^{-6}, 1)$
$8 \leq \Delta t_{TCA} < 12$	$(4.5 \times 10^{-6}, 10^{-3})$	$(1.2 \times 10^{-6}, 1)$
$12 \leq \Delta t_{TCA} < 16$	$(4.0 \times 10^{-6}, 10^{-3})$	$(1.0 \times 10^{-6}, 1)$
$16 \leq \Delta t_{TCA} < 20$	$(2.8 \times 10^{-6}, 10^{-3})$	$(1.0 \times 10^{-6}, 0.68)$
$20 \leq \Delta t_{TCA} < 24$	$(2.2 \times 10^{-6}, 10^{-3})$	$(1.0 \times 10^{-6}, 0.496)$

## 5. CONCLUSIONS

This work focused on quantification of risk to the space environment posed by spacecraft with a special emphasis on satellites which are part of mega-constellations. We introduced a methodology for estimating this risk by computing yearly, per-satellite residual risk. Residual risk was defined in a conceptually simple manner as the risk to a spacecraft which remains even after adherence to a risk mitigation strategy, and the residual risk was modeled in a way which closely resembles how SpaceNav operationally practices maneuver planning. We demonstrated via numerical simulation that residual risk is a function of maneuver execution time,  $\Delta t_{TCA}$ , risk reduction factor,  $\rho$ , and RMM threshold,  $P_m$ , and that each of these three factors plays a significant role in determining residual risk. This result offers a more complete model of spacecraft safety and potential risk to the space environment by studying more than just the RMM threshold  $P_m$ , which has historically been used as a common benchmark in space situational awareness and regulatory compliance literature.

Additionally, we provided an analytical result for estimating the necessary residual risk to ensure the total aggregate collision probability of a satellite constellation of arbitrary size be below a target value. With this analytical formula, we demonstrate that even by assuming a relatively aggressive risk posture results in constellation-wide aggregate collision probabilities which are remarkably large for large satellite constellations, e.g.,  $P_c^{total} = 10^{-1}$  after one year for a constellation of 10 000 satellites with yearly, per-satellite residual risk of  $10^{-5}$ .

## 6. REFERENCES

- [1] 18th Space Control Squadron. Spaceflight Safety Handbook for Satellite Operators. Version 1.5, 2020.
- [2] William H Ailor and Glenn E Peterson. Collision avoidance as a debris mitigation measure. In *55th International Astronautical Congress of the International Astronautical Federation, the International Academy of Astronautics, and the International Institute of Space Law*, pages IAA-5, 2004.
- [3] PJ Blount. Renovating space: The future of international space law. *Denv. J. Int'l L. & Pol'y*, 40:515, 2011.
- [4] Aaron C Boley and Michael Byers. Satellite mega-constellations create risks in low earth orbit, the atmosphere and on earth. *Scientific Reports*, 11(1):1-8, 2021.
- [5] Alan Boyle. Boeing gets fcc approval for 147-satellite constellation. *Space.com*, page 2021, 2021.
- [6] Harriet Brettle, Hugh Lewis, Toby Harris, and Mike Lindsay. Assessing debris removal services for large constellations. In *Proceedings of the 8th European Conference on Space Debris*, 2021.
- [7] Indra Mohan Chakravarti, Radha Govira Laha, and Jogabrata Roy. Handbook of methods of applied statistics. *Wiley Series in Probability and Mathematical Statistics (USA) eng*, 1967.
- [8] Chuan Chen and Wulin Yang. The impact of large constellations on space debris environment and its countermeasures. In *8th European Conference for Aeronautics and Space Sciences (Eucass)*, 2017.
- [9] Federal Communications Commission et al. Technical overview of the hvnet system. *Federal Communications Commission: Washington, DC, USA*, 2021.
- [10] Ido Dagan, Lillian Lee, and Fernando Pereira. Similarity-based methods for word sense disambiguation. *arXiv preprint cmp-lg/9708010*, 1997.
- [11] W.W. Daniel. *Applied Nonparametric Statistics*. Duxbury advanced series in statistics and decision sciences. PWS-KENT Pub., 1990.
- [12] J Foster. A 160 day simulation of space station debris avoidance operations with usspacecom. Technical report, NASA DM3-95-2, Feb, 1995.
- [13] J Foster and J Frisbee. Comparison of the exclusion volume and probability threshold methods for debris avoidance for the sts orbiter and international space station. *NASA Technical Paper*, 214751, 2007.
- [14] James Lee Foster and Herbert S Estes. *A parametric analysis of orbital debris collision probability and maneuver rate for space vehicles*. NASA, National Aeronautics and Space Administration, Lyndon B. Johnson Space . . . , 1992.
- [15] JL Foster. The analytic basis for debris avoidance operations for the international space station. *EUROPEAN SPACE AGENCY-PUBLICATIONS-ESA SP*, 473:441-446, 2001.
- [16] JL Foster, MB Wortham, and JH Frisbee Jr. Iss debris avoidance maneuver threshold analysis. Technical report, NASA/TP-2007-214752, 1999.
- [17] Michael Gould. Facilitating small satellite enterprise for emerging space actors: Legal obstacles and opportunities. In *Legal Aspects Around Satellite Constellations*, pages 29-46. Springer, 2021.

- [18] Doyle T. Hall. Determining appropriate risk remediation thresholds from empirical conjunction data using survival probability methods. *Advances In The Astronautical Sciences*, 171:3439–3456, 2019.
- [19] Caleb Henry. SpaceX submits paperwork for 30,000 more starlink satellites. *Space News*, 15:2019, 2019.
- [20] Felix R Hoots and Ronald L Roehrich. Models for propagation of norad element sets. Technical report, Aerospace Defense Command Peterson AFB CO Office of Astrodynamics, 1980.
- [21] K Kensinger, S Duall, and S Persaud. The united states federal communication commission’s regulations concerning mitigation of orbital debris. In *Proceedings of the 4th European Conference on Space Debris Held*, pages 18–20, 2005.
- [22] Donald J Kessler. *Orbital debris environment for spacecraft designed to operate in low Earth orbit*, volume 100471. National Aeronautics and Space Administration, 1989.
- [23] Heiner Klinkrad. *Space debris: models and risk analysis*. Springer Science & Business Media, 2006.
- [24] Vladimír Kopal. Treaty on principles governing the activities of states in the exploration and use of outer space, including the moon and other celestial bodies. *YB Air & Space L.*, page 463, 1966.
- [25] Christopher Manning and Hinrich Schütze. *Foundations of statistical natural language processing*. MIT press, 1999.
- [26] Jonathan McDowell. Constellation models. *Jonathan’s Space Report*, 2022.
- [27] Darren McKnight, Rachel Witner, Francesca Letizia, Stijn Lemmens, Luciano Anselmo, Carmen Pardini, Alessandro Rossi, Chris Kunstadter, Satomi Kawamoto, Vladimir Aslanov, et al. Identifying the 50 statistically-most-concerning derelict objects in leo. *Acta Astronautica*, 181:282–291, 2021.
- [28] Douglas Messier. Astra space applies to launch more than 13,000 satellites; proposed broadband constellations exceed 79,000 spacecraft. *Parabolic Arc*, page 2021, 2021.
- [29] Jonas Radtke, Christopher Kebschull, and Enrico Stoll. Interactions of the space debris environment with mega constellations—using the example of the oneweb constellation. *Acta Astronautica*, 131:55–68, 2017.
- [30] Shuyi Ren, Xiaohua Yang, Ronglan Wang, Siqing Liu, and Xiaojing Sun. The interaction between the leo satellite constellation and the space debris environment. *Applied Sciences*, 11(20):9490, 2021.
- [31] David Sibert, David Borgeson, Glenn Peterson, Alan Jenkin, and Marlon Sorge. Operational impact of improved space tracking on collision avoidance in the future leo space debris environment. Technical report, SPACE AND MISSILE SYSTEMS CENTER LOS ANGELES AFB CA, 2010.
- [32] Matthew Stevenson, Darren McKnight, Hugh Lewis, Chris Kundstadter, and Rachit Bhatia. Identifying the statistically-most-concerning conjunctions in leo. In *Proceedings of the AMOS Technical Conference*, 2021.
- [33] Starlink Updates. Collision avoidance system. Technical report, SpaceX, 2022.
- [34] David Vallado, Paul Crawford, Ricahrd Hujsak, and TS Kelso. Revisiting spacetrack report# 3. In *AIAA/AAS Astrodynamics Specialist Conference and Exhibit*, page 6753, 2006.
- [35] B Bastida Virgili, JC Dolado, HG Lewis, J Radtke, H Krag, B Revelin, C Cazaux, CAMILLA Colombo, R Crowther, and M Metz. Risk to space sustainability from large constellations of satellites. *Acta Astronautica*, 126:154–162, 2016.